

# **Wiley Analytical Science Virtual Conference**

**November 9-17**

**For the 3rd time, The Wiley Analytical Science  
Conference is back!**

**It's all happening November 9 - 17**

The Wiley Analytical Science Virtual Conference will bring together thousands of researchers and practitioners to share current developments in science and industry. Join for exciting presentations from experts in the fields of analytical and bioanalytical chemistry, pharmaceutical research, materials science, lab automation, and related disciplines.

Register to learn about recent developments & applications in:

- Microscopy
- Spectroscopy
- Mass Spectrometry
- Separation Science
- Much more!

**Register here**

# On the Use of Luminescence Intensity Images for Quantified Characterization of Perovskite Solar Cells: Spatial Distribution of Series Resistance

Daniel Walter,\* Yiliang Wu, The Duong, Jun Peng, Liangcong Jiang, Kean Chern Fong, and Klaus Weber

Perovskite solar cells (PSCs) have made rapid advances in efficiency when fabricated as small-area devices. A key challenge is to increase the active area while retaining high performance, which requires fast and reliable measurement techniques to spatially resolve cell properties. Luminescence imaging-based techniques are one attractive possibility. A thermodynamic treatment of the luminescence radiation from MAPbI<sub>3</sub> and related perovskite semiconductors predicts that the intensity of luminescence emission is proportional to the electrochemical potential in the perovskite absorber, bringing with it numerous experimental advantages. However, concerns arise about the impact of the often-observed hysteretic behavior on the interpretation of luminescence-based measurements. This study demonstrates that despite their hysteretic phenomena, at steady-state perovskite solar cells are amenable to quantitative analysis of luminescence images. This is demonstrated by calculating the spatial distribution of series resistance from steady-state photoluminescence images. This study observes good consistency between the magnitude, voltage-dependence, and spatial distribution of series resistance calculated from luminescence images and from cell-level current–voltage curves and uncalibrated luminescence images, respectively. This method has significant value for the development of PSC process control, design and material selection, and illustrates the possibilities for large-area, spatially resolved, quantitative luminescence imaging-based characterization of PSCs.

## 1. Introduction

Perovskite solar cells (PSCs) are infamous for their abnormal hysteretic, or capacitive, phenomena.<sup>[1,2]</sup> The physical processes that govern this behavior complicate our understanding of charge transport in PSCs, and wide-spread research is dedicated

to unraveling its nature.<sup>[3–6]</sup> Nonetheless, when we consider the electronic band structure, and by extension properties of optical absorption and emission, the widely investigated MAPbI<sub>3</sub> perovskites have so far demonstrated properties consistent with well-ordered, nonexcitonic inorganic semiconductors.<sup>[7,8]</sup> Theoretical and experimental evidence now indicates that MAPbI<sub>3</sub> perovskites are mixed direct–indirect bandgap semiconductors,<sup>[9,10]</sup> in which radiative emission occurs via band-to-band recombination of unbound electron–hole pairs.<sup>[11–13]</sup> Thus, a treatment of the thermodynamic equilibrium of the luminescence radiation predicts that the luminescence photon flux at photon energy,  $E$ , can be modeled by<sup>[14,15]</sup>

$$\phi(E, \mu_{\gamma}, T) = a(E) \phi_{\text{BB}}(E, T) \exp\left(\frac{\mu_{\gamma}}{kT}\right) \approx a(E) \frac{2E^2}{h^3 c^2} \frac{1}{\exp(E/kT)} \exp\left(\frac{\mu_{\gamma}}{kT}\right) \quad (1)$$

where  $a$  is the absorptivity of the medium,  $k$  is the Boltzmann constant,  $\mu_{\gamma}$  is the electrochemical potential of the photons and


$\phi_{\text{BB}}$  the black-body spectrum at absolute temperature  $T$ . Therefore, in the form described in Equation (1), the photon flux is defined in units of photons  $\text{eV}^{-1} \text{m}^{-2} \text{s}^{-1}$ . In a system where the equilibrium occupancy of the conduction and valence bands is modeled by the Maxwell–Boltzmann approximation of Fermi–Dirac statistics, the photon potential,  $\mu_{\gamma}$ , is equal to the separation of the quasi-Fermi energy levels for electrons and holes,  $\Delta\eta$ . The total photon flux is then the integral of Equation (1) over photon energy

$$\Phi(\mu_{\gamma}, T) = \exp\left(\frac{\Delta\eta}{kT}\right) \int a(E) \frac{2E^2}{h^3 c^2} \frac{1}{\exp(E/kT)} dE \quad (2)$$

The model described by Equations (1) and (2) is a generalized form of Planck's Law, which models the spectral intensity of nonthermal (luminescence) radiation.<sup>[14,15]</sup> It has been verified for both direct<sup>[15]</sup> and indirect inorganic semiconductors,<sup>[16]</sup> and thus we can reasonably expect that it will describe the flux of luminescence emission from perovskite materials

Dr. D. Walter, Y. Wu, T. Duong, J. Peng, Dr. K. C. Fong, Prof. K. Weber  
Research School of Engineering  
Australian National University  
Acton, ACT 2601, Australia  
E-mail: daniel.walter@anu.edu.au

Dr. L. Jiang  
Department of Materials Science and Engineering  
Monash University  
Clayton, Victoria 3800, Australia

 The ORCID identification number(s) for the author(s) of this article can be found under <https://doi.org/10.1002/aenm.201701522>.

DOI: 10.1002/aenm.201701522

based on their electronic band structure. As we can see from Equation (2), this model predicts an exponential proportionality between the luminescence intensity and the quasi-Fermi-level separation. Recent experimental evidence for MAPbI<sub>3</sub>-based PSCs has proven consistent with this prediction. For example, Tress et al.<sup>[12]</sup> closely approximated MAPbI<sub>3</sub> electroluminescence (EL) emission spectra with this model from which an upper limit on open-circuit voltage was determined using Rau's reciprocity relationship.<sup>[17]</sup> El-Hajje et al. extended reciprocity analysis to hyperspectral imaging, which used high-resolution confocal microscopy to capture luminescence spectra, which in turn quantified the local photovoltage.<sup>[18]</sup> Finally, Hameiri et al. demonstrated a proportionality between PL intensity and the open-circuit voltage consistent with this model for a MAPbI<sub>3</sub>-based PSC.<sup>[13]</sup>

However, the experimental advantages of Equation (2) have yet to be fully exploited for PSC characterization, most notably through its potential for the translation of the steady-state luminescence intensity to quantitative cell-level parameters. It is important to emphasize that the analysis presented here focuses on the steady-state luminescence emission of PSCs. Of course, transient luminescence data have become one of the workhorse tools for characterization of the electronic properties of perovskite films, by providing an insight into the dynamics of charge-carrier recombination.<sup>[19,20]</sup> However, these techniques cannot be considered suitable for large-area analyses. Steady-state luminescence intensity, on the other hand, can be readily captured in an imaging configuration with resolutions from micrometers to millimeters, resolving the full cell area in less than a second. To date, a handful of studies have used luminescence imaging of PSCs to reveal the relative distribution of nonradiative recombination,<sup>[21,22]</sup> the resistance to charge carrier injection and extraction (i.e., series resistance)<sup>[23]</sup> and perovskite-silicon tandem structures.<sup>[24]</sup> Yet one of the major advantages of the generalized Planck law of Equation (2) is the ability to translate luminescence intensity to quantitative device parameters through the fundamental relationship between luminescence and electrochemical potential. Notably, this relationship has formed the basis of valuable methods of characterization in silicon photovoltaic research. Through the imaging of luminescence intensity, experimentalists have spatially resolved a wide range of material and device properties, including the effective minority charge carrier lifetimes,<sup>[25]</sup> voltage potential,<sup>[26]</sup> dopant distribution,<sup>[27]</sup> and diffusion length,<sup>[28,29]</sup> among other parameters. Such experimental capabilities are obviously of interest for perovskite photovoltaics as cell areas increase and spatial information becomes of greater importance in tracking the uniformity of process conditions or regions of degradation.

Therefore, in this work, we present further evidence for—and extend the practical utility of—the diagnostic power of the generalized Planck law for the steady-state large-area quantitative characterization of PSCs. We show that despite the transient conditions that precede steady-state, the intensity of steady-state luminescence emission is consistent with Equation (2) for both MAPbI<sub>3</sub> PSCs and a multication Cs<sub>0.07</sub>Rb<sub>0.03</sub>FA<sub>0.765</sub>MA<sub>0.135</sub>PbI<sub>2.55</sub>Br<sub>0.45</sub> PSC,<sup>[30,31]</sup> and thus can be used to quantify valuable cell-level parameters. The consideration of two markedly different perovskite structures, including

a well-established material and a cutting-edge mixture, is evidence for a broad applicability of this analysis to PSCs.

We demonstrate the utility of the generalized Planck law through the calculation of local series resistance, which is validated against cell-level current voltage measurements and uncalibrated luminescence images. The series resistance is a parameter, which has significant influence on the fill-factor, and therefore the photovoltaic conversion efficiency of a solar cell. Previous analysis of EL emission at cell level for a MAPbI<sub>3</sub> PSC has indicated that the emission is sensitive to series resistance.<sup>[13]</sup> In PSCs, series resistance is known to be susceptible to suboptimal conditions at the perovskite–transport layer interfaces,<sup>[32–34]</sup> and can be increased by the delamination of the transport layers, which may be linked to ion migration.<sup>[23]</sup> Consequently, a major focus of PSC research is the identification of high-efficiency charge-carrier-selective transport layers.<sup>[35–38]</sup> High throughput quantification of the magnitude and spatial distribution of the series resistance will assist these efforts to identify optimal materials and fabrication techniques.

## 2. Results and Discussion

### 2.1. Theoretical Model

A brief introduction to the method by which the local series resistance is calculated from steady-state luminescence images is warranted, as it lays out the assumptions that underpin the following analysis. This method, described by Kampwerth et al.,<sup>[39]</sup> was originally derived for silicon photovoltaics. For this calculation, series resistance is defined per the widely used equivalent circuit model of Figure 1. It is therefore a lumped parameter, capturing all contributions to voltage loss between the perovskite absorber and the potential measured at the terminals, both ohmic and voltage dependent.<sup>[40,41]</sup> The voltage dependence of the series resistance can be resolved via methods that calculate resistance at specific terminal voltages, such as those used in this work.<sup>[39,41]</sup> For the luminescence-based calculation of the local series resistance, the cell is treated as a 2D parallel network in which each pixel is modeled according to the equivalent circuit. However, this method simplifies the equivalent circuit by treating the parasitic current flow elements, marked by the red box of Figure 1, as a

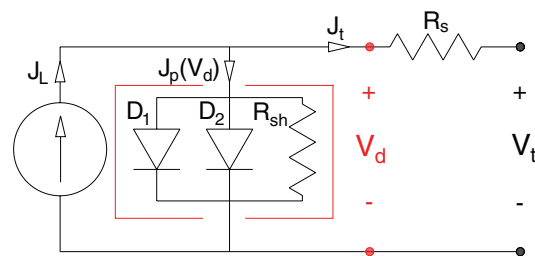


**Figure 1.** Equivalent circuit assumed in the luminescence-based  $R_s$  calculation. The red-bordered region represents the parasitic elements of the circuit—typically parallel diodes and a shunt resistance—that are treated as a “black-box” current flow function,  $J_p(V_d)$ , dependent only on the diode voltage,  $V_d$ .  $V_d$  differs from the voltage measured at the cell terminals,  $V_t$ , by the voltage drop across the series resistance,  $R_s$ .



single “black-box” element. The current flow into this element is approximated as a function dependent only on the potential across it. This internal potential, known as the **junction or diode voltage ( $V_d$ )**, differs from the terminal potential ( $V_t$ ) by the voltage drop across the series resistance. Under this simplified circuit model, the series resistance is calculated differentially by identifying two operating conditions, defined by their respective photocurrent density,  $J_L$ , and terminal voltage,  $V_t$ , for which  $V_d$  is constant. Consequently, we assume that the current flow,  $J_p$ , is equal under these conditions. Once these operating conditions are identified, the series resistance follows directly from the difference in voltage and current at these two operating points (defined as points 1 and 2). The current flow through the parallel parasitic elements is canceled out by the comparison between the two operating points

$$r_s = \frac{V_{t2} - V_{t1}}{J_{L1} - J_{L2}}; V_{d1} = V_{d2} \quad (3)$$

The terminal voltage is readily accessible to the experimentalist; the internal voltage, however, is not. We see then the advantage of the link between voltage and luminescence flux defined by the generalized Planck law. We can substitute the inaccessible diode voltage with the accessible luminescence intensity, and **seek operating points for which the luminescence intensity is constant** (i.e., where  $V_{d1} = \Phi_1 = \Phi_2 = V_{d2}$ , where  $\Phi$  is the luminescence intensity). Series resistance at each pixel is then calculated from Equation (3). Because of the impractical demands of identifying the necessary operating points such that  $\Phi_1 = \Phi_2$  for every pixel of a luminescence image, an **interpolation method is employed**, which compares multiple  $\Phi(V_t)$  data points from one illumination level to a single  $\Phi(V_t)$  **measurement at a second, lower illumination level**. For more details of this method, we recommend the original publication.<sup>[39]</sup>

In the context of PSCs, the advantage of the equivalent circuit assumptions of Figure 1 is that we can afford some ignorance about the nature of the steady-state current flow through the parallel, parasitic elements, so long as it can be closely approximated as a function only of voltage. These components often consist of one or more parallel diodes, representing bulk and junction recombination, and a shunt resistor, representing parasitic current paths parallel to the junction. The recombination pathways are parameterized by one or two recombination prefactors,  $J_{01,2}$ , and the ideality factors,  $n_{1,2}$ . It is uncertain what parameters best describe a perovskite solar cell at steady state, and this may vary between device structures, perovskite compositions and even laterally across individual cells. However, in this calculation, each pixel is compared to itself at different operating conditions that produce equivalent internal voltages, and therefore the  $J_0$  and  $n$  terms are canceled out. This calculation thus minimizes experimental error associated with calculating these parameters directly,<sup>[42,43]</sup> and increases applicability across types of PSCs.

Finally, our confidence in the following analysis is increased by simultaneous calculations, using the same measurement protocol, of a “model” photovoltaic device: a high-efficiency (23.1% conversion efficiency, 0.707 V open-circuit voltage) interdigitated back contact silicon solar cell.<sup>[44]</sup> The models of Equation (2), and Figure 1, are well established for this solar

cell technology. Therefore, in the discussion to follow, we present alongside the PSC analysis equivalent calculations from this silicon cell. The purpose of this characterization is to provide a reference against which we can verify our methods to validate the calculations of local series resistance for the PSCs and gauge the ‘ideality’ of their experimental behavior.

## 2.2. Series Resistance Calculations

Our calculations of series resistance, using cell-level current density–voltage ( $J$ – $V$ ) measurements and PL images, use measurements taken at steady-state conditions for a planar MAPbI<sub>3</sub> and mesoporous mixed-cation PSC structures. The cells were biased from **open- to short-circuit voltage**, and both cells exhibited a slow stabilization of photocurrent (hysteresis) after a change in external bias. Steady-state conditions were defined by  $dI/dt < 10 \mu\text{A cm}^{-2} \text{ s}^{-1}$ . The measurement conditions were chosen to satisfy the needs of the luminescence-based and global series resistance calculations, and were deliberately truncated to minimize measurement time and the potential for degradation of the PSCs. **Figure 2** plots the steady-state  $J$ – $V$  relationships for the perovskite and silicon solar cells. These measurements were taken under monochromatic illumination in the luminescence imaging systems. Measurements of the  $J$ – $V$  characteristics of the cells under AM1.5G illumination with a 50 mV s<sup>−1</sup> reverse voltage scan are presented in Figure S1 (Supporting Information). Under AM1.5G illumination, the multication cell had a one-sun equivalent power conversion efficiency of ≈17% with an open circuit voltage of 1.15 V and fill factor (FF) of 0.67, and the MAPbI<sub>3</sub> cell was ≈11.9% efficient, with an open circuit voltage of 0.93 V and a FF of 0.60. A superficial examination of the shape of the  $J$ – $V$  curves indicates that both PSCs are influenced by **relatively high series resistance**, evidenced by the relatively shallow gradient beyond open circuit. This is best exemplified by comparison to the low-series resistance silicon  $J$ – $V$  curve, for which current decreases steeply beyond maximum power point (FF = 0.79).

**Figure 3** shows luminescence images of the multication, MAPbI<sub>3</sub> and silicon solar cells. Shown are **PL images with the cell biased at maximum power point**, and **EL images biased at maximum power point current**. For the multication cell, the images are dominated by bands of alternating high and low intensity signal, likely reflecting strands of differing electronic quality produced by spin coating of the perovskite layer. Such **features have been observed in previous luminescence imaging of PSCs**<sup>[22]</sup> and are regularly measured in our laboratory on PSC devices incorporating TiO<sub>2</sub> mesoporous scaffolds. The planar MAPbI<sub>3</sub> cell is devoid of these features but exhibits localized regions with large variations in luminescence intensity, which indicates **substantial heterogeneity in the perovskite material or cell structure**. Conversely, the silicon cell is almost featureless, consistent with the high-quality structure of float-zone crystalline silicon and well-controlled processing.

The images of Figure 3 can provide an indication of the distribution of series resistance across the cell. The intensity of each pixel reflects the **depth-averaged steady-state charge carrier density at that pixel**, as the rate of radiative recombination is directly proportional to the product of the electron and hole

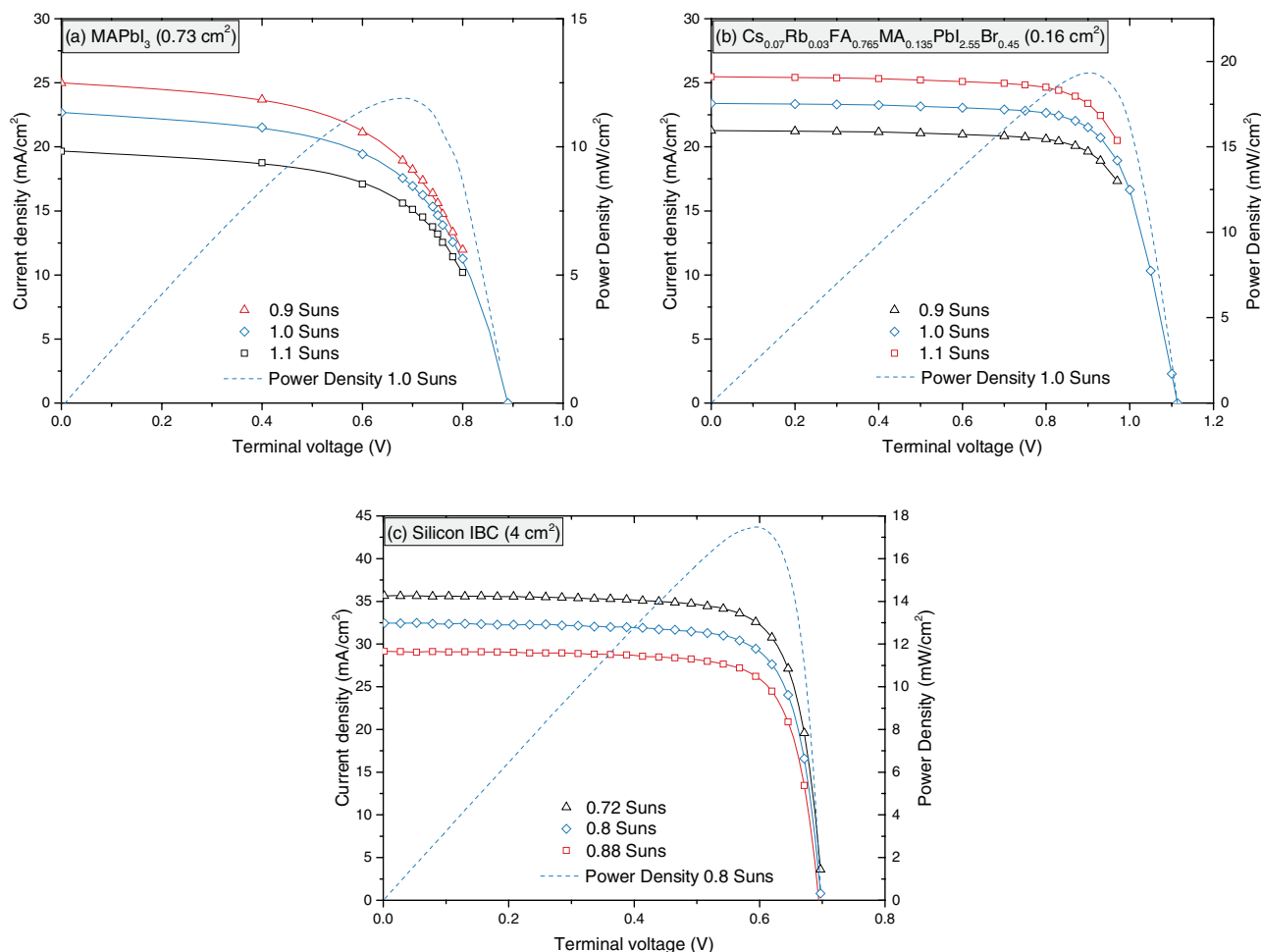


**Figure 2.** Steady-state  $J$ - $V$  curves of a) multication PSC, b) MAPbI<sub>3</sub> PSC, and c) silicon IBC solar cell. Both PSC solar cells had slow photocurrent responses (hysteresis), and so the data points were truncated to minimize the measurement duration and the potential for cell degradation. For the silicon IBC cell, the measurement system limited the maximum illumination to  $\approx 0.9$  suns equivalent. Three illumination levels targeting 1 sun  $\pm 10\%$  illumination are desired for the global series resistance calculations (see text).

concentrations. Thus, when the cell is externally biased, series resistance can influence the total luminescence intensity by influencing the steady-state carrier populations, other things being equal. **High series resistance limits charge-carrier injection under EL conditions** (i.e., unilluminated, externally biased) and will therefore reduce the steady-state population of charge carriers. By comparison, under biased PL conditions (illuminated, with current extraction through the cell terminals), high series resistance limits charge extraction and increases the steady-state luminescence signal. Therefore, where series resistance plays a measurable role in influencing charge extraction or injection, we can expect an anticorrelation between the biased-PL and EL signal. By this argument, it is probable that the banded features of the multication cell do not indicate variations in local series resistance, as the relative signal levels are correlated between the EL and biased PL conditions. The same can be said for the loop-like low-signal region in the bottom half of the cell. For the MAPbI<sub>3</sub> cell, however, the localized bright regions of the biased PL image correspond to low-signal regions of the EL image, pointing toward large variations in series resistance. Finally, the silicon IBC cell is relatively

featureless, consistent with its high-quality crystal structure and well-controlled processing.

Before we proceed to the series resistance calculation, however, we first wish to confirm that our measurement protocol **accurately reveals the separation of the quasi-Fermi levels, and therefore internal potential, of the perovskite absorber.** This measurement is complicated by significant luminescence emission from the **FTO/TiO<sub>2</sub> surface layers,** which is voltage-independent, scales linearly with illumination and is independent of current (see Figure S2, Supporting Information). This signal is captured by taking PL images of the perovskite solar cells at short-circuit conditions, at which we assume the luminescence emission from the perovskite layer is negligible. This image is then subtracted from all images taken at positive electrical bias at the same level of illumination.

With this correction, we may expect the resulting intensity of the detected radiative emission from the perovskite solar cells to be, by Equation (2), **proportional to  $\exp(\Delta E_F/kT)$ .** We can attempt to validate this relationship by simultaneous measurement of the terminal voltage and the luminescence signal under open-circuit conditions across a range of illumination

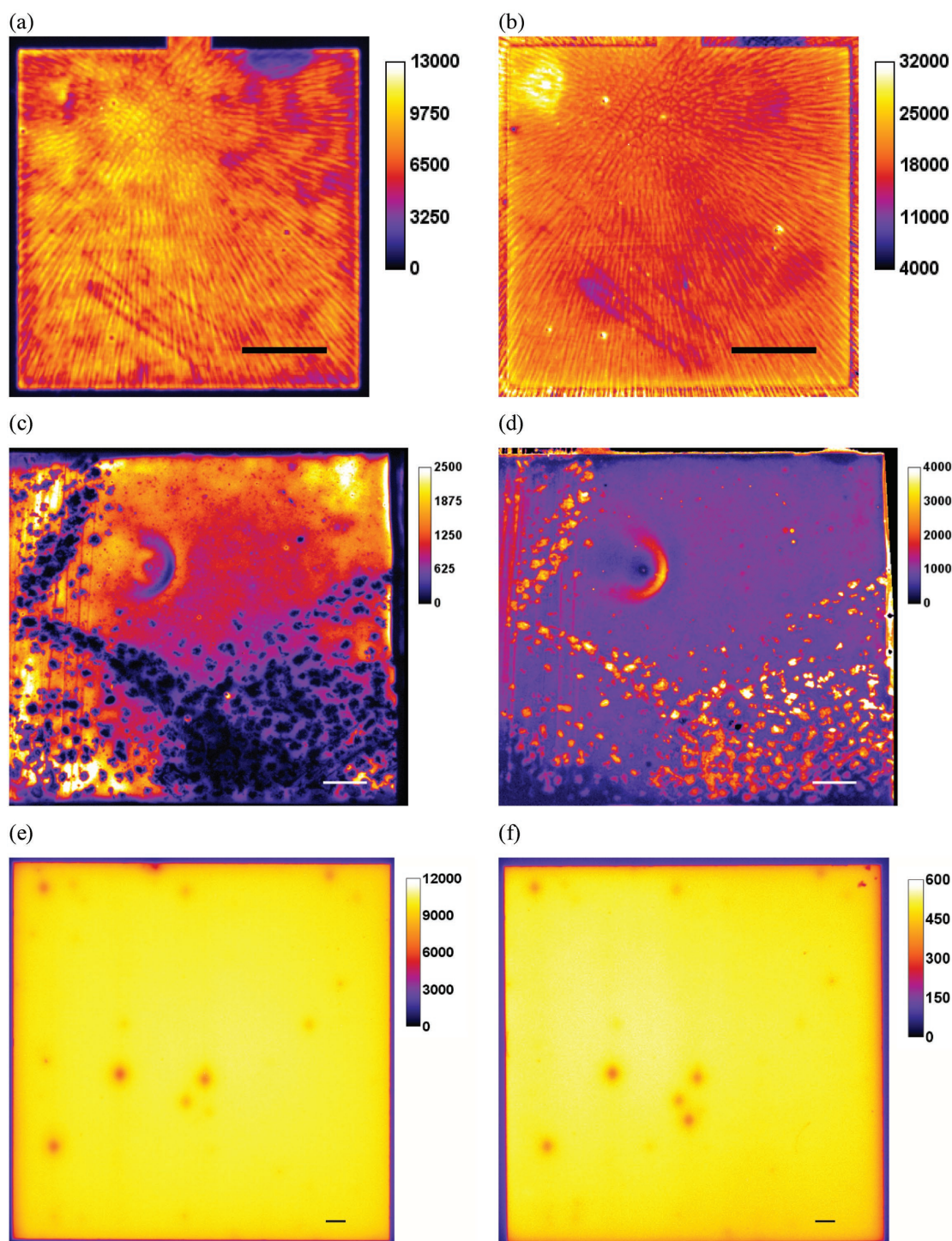


**Figure 3.** EL image (left column) and biased-PL image (right column) for a,b) multication PSC, c,d) MAPbI<sub>3</sub> PSC, and e,f) silicon IBC solar cell. These images reveal the steady-state distribution of excess carrier density, and the two image conditions can indicate the influence of series resistance effects. An anticorrelation in the signal levels points toward regions in which the steady-state carrier population is influenced by series resistance. Scale bars represent 1 mm, units are counts per second (an arbitrary unit of luminescence intensity).

levels. Under open-circuit conditions, the quasi-Fermi levels are roughly flat due to the absence of net current flow in the device. Thus, the depth-averaged quasi-Fermi separation closely approximates the quasi-Fermi level separation at the electron

and hole contacts, which is probed at the cell terminals. For the silicon solar cell, for which we know the generalized Plank law describes the intensity of luminescence emission,<sup>[45]</sup> the proportionality of the PL intensity–open-circuit voltage relationship



over an illumination range of  $\approx 0.03$  to 0.9 suns could not be distinguished from the prediction of Equation (2) (Figure S3, Supporting Information).

The presence of hysteresis, however, complicates our ability to accurately validate the predictions of the generalized Planck law for the MAPbI<sub>3</sub> PSC. We have previously shown that transient changes in open-circuit voltage that precede steady state can result in a “decoupling” between the luminescence signal (and therefore the internal potential) and the open-circuit voltage measured at the cell terminals.<sup>[46]</sup> We ascribed this phenomenon to the redistribution of ions in the presence of the electric field induced by the cell potential, which modulates conductivity of the favored charge carrier at the transport layer interfaces. In conjunction with nonnegligible interface recombination, this results in a time-varying quasi-Fermi level of the favored charge carrier at the interface. The terminal voltage is reduced while having minimal impact on the quasi-Fermi levels in the perovskite absorber. Consequently, as the ionic population redistributes toward equilibrium, the terminal voltage will gradually change, but the luminescence signal will remain roughly constant, an apparent “violation” of theoretical predictions. An example of this behavior for the MAPbI<sub>3</sub> PSC is plotted in Figure 4a. However, despite the abnormal PL–V<sub>oc</sub> transience that precedes steady state, once the cell reaches steady-state conditions, the final PL–V<sub>oc</sub>—measured over an illumination range spanning roughly 1.5 orders-of-magnitude—is closely proportional to  $\exp(V_{oc}q/kT)$  as predicted by Equation (2). For the MAPbI<sub>3</sub> PSC, we extract a coefficient of proportionality of  $1.07 \pm 0.14$ . By way of reference, the equivalent calculation for silicon yields a coefficient of  $1.01 \pm 0.04$ . This calculation for a MAPbI<sub>3</sub> PSC concurs with previous literature,<sup>[13]</sup> and the transient phenomenon we observe is a possible explanation for the reported necessity in that work to light soak the cell at open-circuit conditions in order to observe the expected PL–V<sub>oc</sub> relationship. We also observe excellent agreement for the steady-state PL–V<sub>oc</sub> relationship of the multication

cell, of  $1.01 \pm 0.07$ . For this cell, the stabilization of open-circuit voltage following illumination was too rapid ( $<3$  s) for our experimental system to resolve any transient abnormalities. Therefore, we conclude that although the hysteresis phenomena of these PSCs may complicate the interpretation of transient luminescence signals, at steady-state conditions we can confidently conclude that the generalized Planck law describes the relationship between the electrochemical potential of the perovskite absorber and the detected luminescence intensity, a key requirement for our subsequent calculations.

### 2.3. Validation of the Local Series Resistance Calculations

We now turn to the calculation of local series resistance itself. We calculated series resistance images at terminal voltages close to the maximum power point of each cell, to provide data relevant to the expected operating conditions. Figure 5 presents maps of series resistance for the three cell types. Our first step in the validation of these images is consistency with the global series resistance calculated from cell-level  $J$ – $V$  data. For this calculation, we choose to use the so-called multi-light method (MLM),<sup>[41]</sup> an extension of the widely used double-light method<sup>[47]</sup> for series resistance measurements of solar cells. We have adopted the MLM—despite several techniques available to measure global series resistance<sup>[27,29]</sup>—because the data requirements directly overlap with those of the PL series resistance calculation. Thus, we can base our calculation of global series resistance on data acquired from the same measurement protocol as the PL images. This approach is motivated by observations that hysteresis in PSCs can influence even sequential measurements,<sup>[48]</sup> thus reducing the confidence in comparisons between data from two measurement procedures. In addition, other series resistance characterization methods, such as a comparison between a dark and light  $J$ – $V$  curve,<sup>[40]</sup> require cell measurements under very different operating conditions. Our

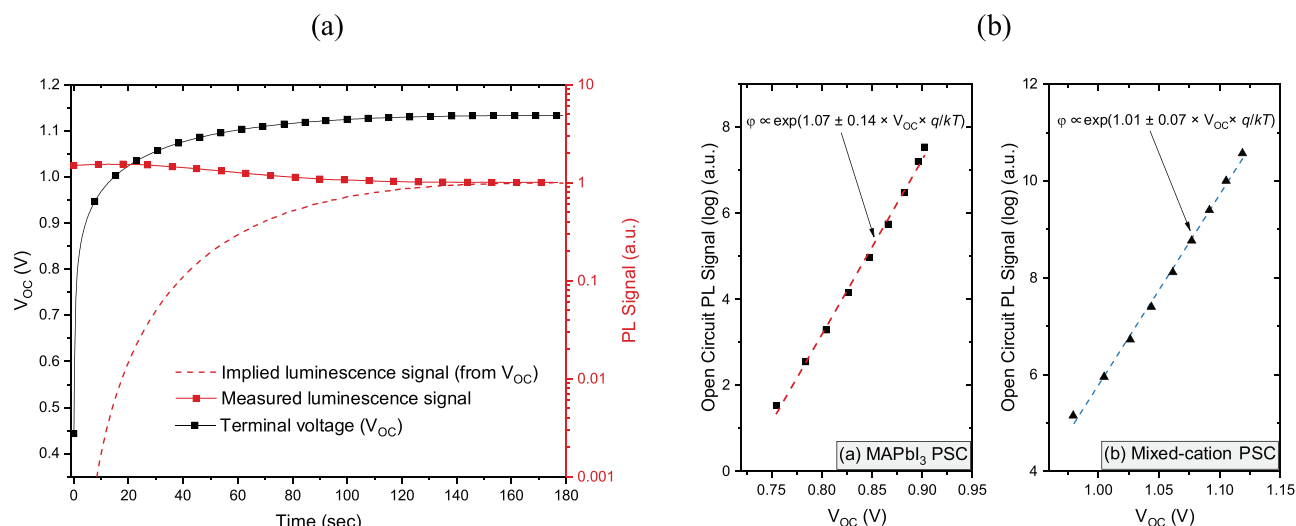


**Figure 4.** a) In response to illumination, hysteresis in the MAPbI<sub>3</sub> PSC results in a transient relationship between  $V_{oc}$  and the luminescence signal that deviates from the predictions of Equation (1). b) However, once at steady-state conditions, the PL– $V_{oc}$  relationship is a close match to Equation (2) over an illumination range of roughly 1.5 orders of magnitude (coefficient of proportionality of  $1.07 \pm 0.14$ ). A calculation for the multication PSC reveals a similar coefficient of  $1.01 \pm 0.07$ .

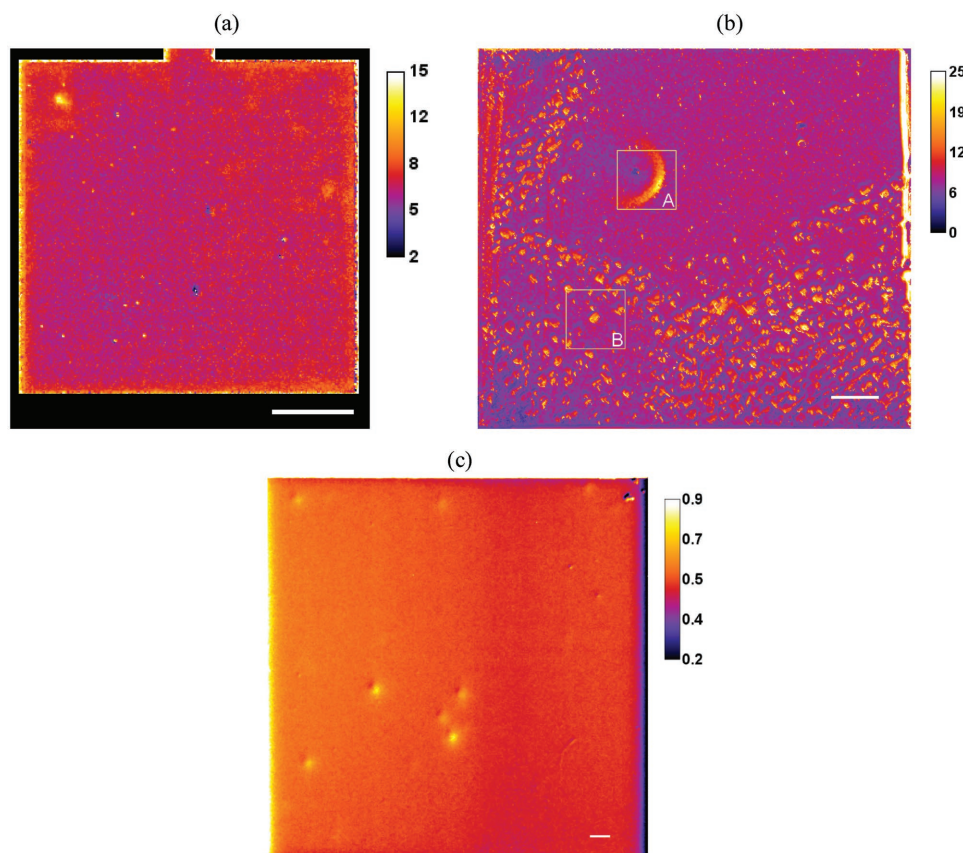


**Figure 5.** Maps of series resistance at approximately the maximum power point terminal voltage for a) multication PSC, b) MAPbI<sub>3</sub> PSC, and c) silicon IBC. Scale bar represents 1 mm, units are  $\Omega \text{ cm}^2$ .

relative uncertainty about the nature of hysteresis processes again reduces confidence in the comparison between such measurements, as they may represent fundamentally different operating conditions. For this comparison, we are also required to aggregate global resistance from the local series resistance values. Therefore, we computed the arithmetic mean resistance of each series resistance image, which followed the prescription of Michl et al.<sup>[53]</sup> Michl and co-workers found that the mean resistance—in contrast to the aggregation of local resistances by treating the cell as a network of parallel resistors—gave the closest agreement with the true value, which they determined from simulations using a complex circuit model.

**Figure 6** plots the global and aggregated local series resistance as a function of the terminal voltage. The series resistance data of the silicon solar cell, the reference case for this analysis, shows that the mean of the spatially determined series resistance agrees in both magnitude and voltage dependence with the cell-level series resistance. This is a good indication that we can expect agreement between the two calculations for the PSCs. And indeed, both PSC cells exhibit close agreement between aggregate and global series resistance within the margin of error of the calculations. In addition to the data of Figure 3, this is strong evidence that the PL signal is a reliable gauge of the internal potential of the cells, and therefore of our ability to accurately quantify the local series resistance from PL images.

Although the average resistance values are consistent, our next concern is consistency of the spatial information revealed by the series resistance images. As previously discussed, we expect agreement between regions of high and low local series resistance, and the regions identified as influenced by series resistance via anticorrelation between EL and biased PL luminescence intensity. Based on a preliminary comparison of the EL and biased PL images, we predicted that the banded luminescence signal variation in the multication PSC may not reflect regions in which series resistance differed, and this is indeed what we observe. In fact, most the localized features resolved in the EL and PL images of the multication PSC are calculated to have no measurable influence on series resistance. Instead we are left to conclude that **these regions reflect significant variations in nonradiative recombination activity, but do not influence current flow into or out of these regions, for example by influencing the quality of contact between the perovskite layer and the charge-selective transport layers.** The series resistance image therefore reveals information about the cell's performance that is not clearly demonstrated through raw luminescence images, emphasizing the additional diagnostic capability of this analysis. Except for a handful of localized regions, the uniformity of the series resistance for the multication cell is **high, pointing toward spatially uniform contact quality.** However, the corollary result is that this cell structure suffers from generally high series resistance, which at approximately  $6 \Omega \text{ cm}^2$



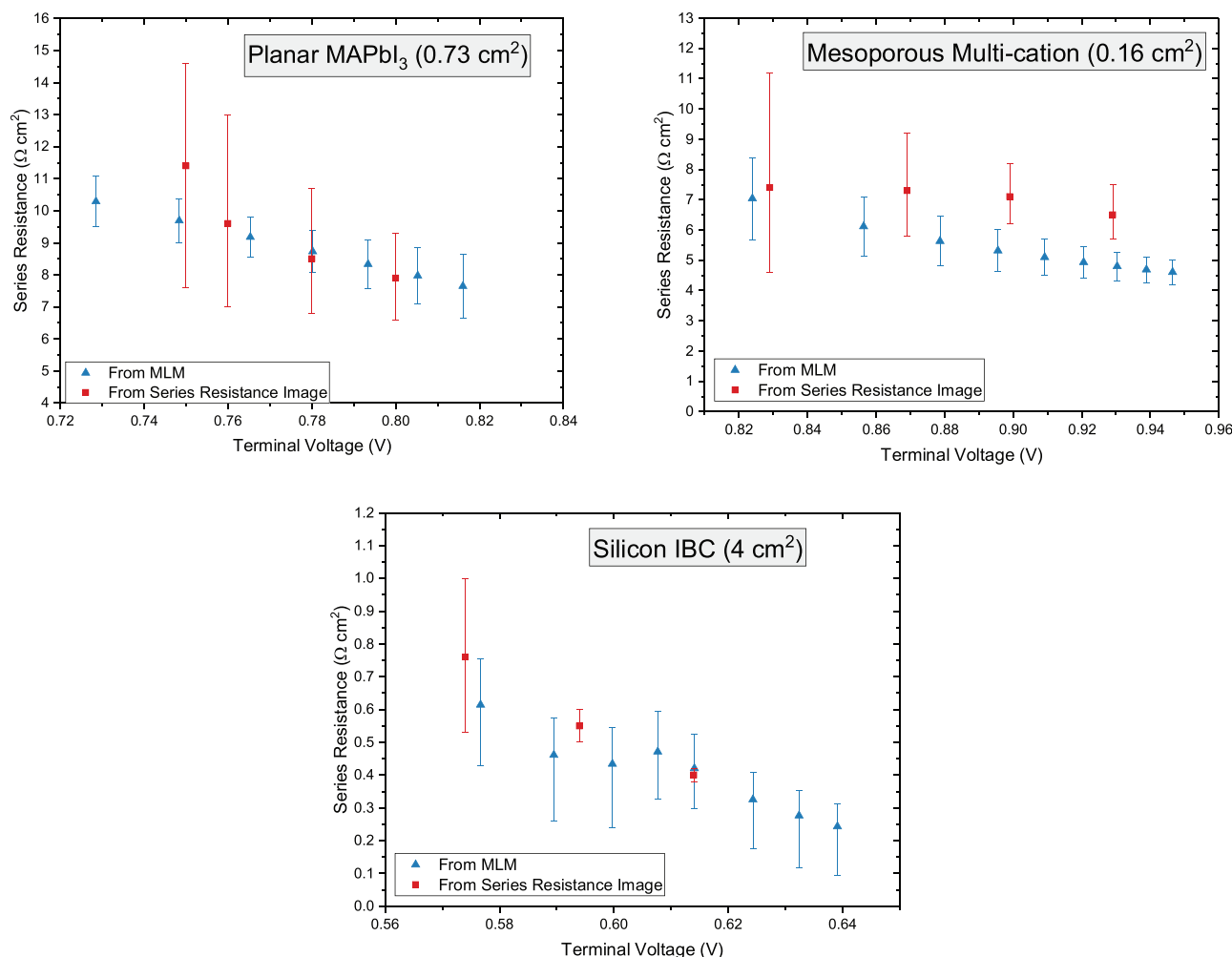


**Figure 6.** Comparison of aggregate local series resistance and global series resistance for a) MAPbI<sub>3</sub> PSC, b) multication PSC, and c) silicon IBC solar cell.

at maximum power point, is roughly an order of magnitude higher than the high-efficiency silicon solar cell.

In the case of MAPbI<sub>3</sub> cell, however, the significant material heterogeneity is shown to strongly affect the local series resistance, again consistent with PL and EL comparisons. This impact can be quantified thanks to this series resistance calculation, showing local values of series resistance as high as  $25 \Omega \text{ cm}^2$  relative to the background level of  $\approx 10 \Omega \text{ cm}^2$ . We also see that consistency between the series resistance calculation and the EL and biased PL images holds for qualitatively different regions, such as the ring-like defect marked in region A, and the localized, spot-like features that dominate three quadrants of the cell, as exemplified in region B. The feature of region A is likely the result of the pipetting of the liquid perovskite precursor, revealing an impact of the fabrication method on cell performance. The large macroscale variation in series resistance is consistent with variations in carrier transport in MAPbI<sub>3</sub> PSCs observed previously.<sup>[18]</sup> Finally, we note here that the resolution of the imaging system, at  $\approx 225 (15 \times 15) \mu\text{m}^2$  per pixel is too coarse to reveal grain-by-grain variations in series resistance, and is instead averaging the resistance of many sub pixel-scale grains.

This analysis demonstrates the ability of a quantified, steady-state luminescence-based calculation to reveal information that is not easily accessible from raw luminescence images, or indeed from other measurement techniques. Although other works have used submicron scale techniques to identify variations in series resistance, none have yet quantified this variation, nor presented a technique that can capture large areas in a practical length of time. For this example, an obvious application is the ability to separate contributing factors to low luminescence signals, thereby distinguishing nonradiative recombination from series resistance effects and diagnosing process uniformity issues. It is also notable that the absolute levels of series resistance for the PSCs measured in this work are roughly an order-of-magnitude higher than a high efficiency silicon solar cell. Admittedly, the MAPbI<sub>3</sub> cell, at 12% efficiency, is not an outstanding example of the technology. However, the multication cell demonstrates low hysteresis and a high open-circuit voltage. This illustrates the extent of the possible improvements in performance that can be realized from optimized transport layer interfaces with reduced resistance to current flow. While the spatial uniformity of charge extraction is

good, there may still be scope for fundamental improvements in the cell structure itself. The technique demonstrated in this work will provide a valuable diagnostic tool in the support of this goal.

### 3. Conclusion

We have demonstrated how the generalized Planck law, which models the relationship between the electrochemical potential and luminescence intensity of a perovskite semiconductor, can be used to quantify device-level properties in both a MAPbI<sub>3</sub> and multication perovskite solar cell. We illustrate the utility of this relationship via the calculation of steady-state local series resistance, which is validated on two fronts. First, the magnitude of the local series resistance is shown to be in close agreement in magnitude and voltage dependence with cell-level calculations from global current–voltage data. Second, quantitative spatial variations in local series resistance are found to be consistent with uncalibrated electroluminescence and photoluminescence images. The validation of these calculations across two different perovskite mixtures with qualitatively different features points to a broad applicability of this approach. In aggregate, the evidence presented in this work allows us to confidently conclude that steady-state luminescence imaging presents exciting possibilities for quantified, spatially resolved, large-area characterization of perovskite solar cells, which promises to be an invaluable tool for future development of this promising photovoltaic technology.

### 4. Experimental Section

**Planar CH<sub>3</sub>NH<sub>3</sub>PbI<sub>3</sub> Solar Cell:** Full details on the preparation method of the MAPbI<sub>3</sub> cell are described elsewhere.<sup>[46]</sup> It consists of the widely investigated structure of FTO/compact-TiO<sub>2</sub>/CH<sub>3</sub>NH<sub>3</sub>PbI<sub>3</sub>/spiro-OMETAD/Au. The active cell area was ≈0.73 cm<sup>2</sup>. Briefly, a compact layer of TiO<sub>2</sub> (≈50 nm thick) was spin coated on FTO glass using from a titanium isopropoxide–HCl precursor. The layer was sintered at ≈500 °C in ambient conditions. The planar MAPbI<sub>3</sub> layer was formed from mixed halide precursors of PbI<sub>2</sub> (1 M) and CH<sub>3</sub>NH<sub>3</sub>I (1 M), which were dissolved in a mixed solvent of *N,N*-dimethylformamide (0.7 mL) and dimethyl sulfoxide (0.3 mL). The perovskite precursor was spin coated, during which chlorobenzene (50 μL) was pipetted into the spinning solution. The film was then annealed at ≈100 °C for 15 min on a hotplate in a glovebox. After cooling, the spiro-OMETAD layer was spin coated, and the cell was contacted with thermally evaporated gold. Finally, the cell was fully encapsulated using the method described by Han et al.,<sup>[32]</sup> which has demonstrated improved stability for CH<sub>3</sub>NH<sub>3</sub>PbI<sub>3</sub> PSCs under high temperature and humidity.

**Planar Cs<sub>0.07</sub>Rb<sub>0.03</sub>FA<sub>0.765</sub>MA<sub>0.135</sub>PbI<sub>2.55</sub>Br<sub>0.45</sub> Solar Cell:** The Cs<sub>0.07</sub>Rb<sub>0.03</sub>FA<sub>0.765</sub>MA<sub>0.135</sub>PbI<sub>2.55</sub>Br<sub>0.45</sub> perovskite precursor solution contains 1.2 M lead iodine (PbI<sub>2</sub>, 99%, Sigma Aldrich), 1.1 M formamidinium (FAI, Dyesol), 0.2 M lead bromide (PbBr<sub>2</sub>, 99.999%, Sigma Aldrich), 0.2 M methylamine bromide (MABr, Dyesol), 0.091 M cesium iodine (CsI, 99.999%, Sigma Aldrich), and 0.039 M rubidium iodide (RbI, 99.9%, Sigma Aldrich) in 1 mL anhydrous DMF:DMSO (4:1, v/v, Sigma Aldrich). It was deposited by a two-step spin coating program: first at 2000 rpm with a ramp of 200 rpm s<sup>−1</sup> for 10 s, and then at 6000 rpm with a ramp of 1000 rpm s<sup>−1</sup> for 10 s. More details on the interface structure will be provided in a forthcoming publication.<sup>[49]</sup>

**Silicon IBC Solar Cell:** The silicon IBC cell was fabricated according to a method described elsewhere.<sup>[44]</sup> The cell efficiency measured via an

in-house calibrated AM1.5G spectrum was 23.1%, with *V*<sub>oc</sub> of 707 mV, *J*<sub>sc</sub> of 41.6 mA cm<sup>−2</sup> and a fill factor of 78.5% (Figure S1, Supporting Information). Maximum power point voltage was 594 mV. The active cell area was defined by an aperture mask measuring 1.98 × 1.98 cm<sup>2</sup>. The light *J*–*V* and PL images were captured via the same method as described for the PSC, albeit without the need to accommodate any measurable hysteresis effects. The cell was measured in a BT Imaging LIS R1 tool, which uses 808 nm laser illumination. The cell was mounted on a temperature controlled stage, and cell temperature was maintained within 25 ± 0.7 °C. Imaging was performed with a magnification lens with a per-pixel resolution of ≈26 × 26 μm<sup>2</sup> and a 1050 nm short-pass filter to reduce photon-spread in the silicon CCD detector.<sup>[50]</sup>

**Steady-State *J*–*V* Curves:** Luminescence images and *J*–*V* data at steady state were used to calculate both global and local values of series resistance, respectively. The cells were biased and the photocurrent recorded with a Metrohm Autolab PGSTAT128N potentiostat. Illumination was provided by Lumileds blue light LEDs with a peak wavelength of emission of 450 nm and a FWHM of ≈20 nm. The LEDs were filtered through Semrock FF01-451 band pass filters (pass-band: 400–500 nm) to eliminate the LEDs' long wavelength tail of emission, which was detectable up to 1000 nm. Images were captured using a Princeton Instruments Pixis 1024 camera with a Peltier-cooled (−70 °C) silicon CCD detector. The pixel resolution is 14.6 ± 0.1 μm. The camera was filtered by a long pass filter to eliminate stray short-wavelength light.

The current–voltage measurement conditions, defined by cell bias and illumination level, were chosen to satisfy the needs of the luminescence characterization technique as well as the MLM for global series resistance calculation. Current and voltage were measured by adjusting cell bias at discrete intervals from near open-circuit through to short-circuit and allowing the cell to reach steady state at each operating point before capturing the luminescence image. Cell current was measured at steady-state. Steady state was defined as a rate-of-change of photocurrent of less than 10 μA s<sup>−1</sup>. We note that over no practical measurement duration did the rate-of-change of photocurrent ever reach 0 A s<sup>−1</sup>. The MAPbI<sub>3</sub> cell was mounted onto a fan cooled stainless steel plate. The perovskite temperature was not actively monitored, but an infrared thermometer indicated that the surface temperature of the perovskite cell rose by ≈7 °C over the course of the measurement. The multication cell was unencapsulated, and contacted through a custom housing that maintained cell temperature at 25 ± 1 °C. The cell was held in an N<sub>2</sub>-purged atmosphere throughout the measurement.

The cell bias points were deliberately truncated to minimize measurement time and the risk of cell degradation, with a finer step of voltage used around maximum power point for improved accuracy of the MLM calculation, and a coarser step as the bias approached short circuit. Illumination levels of 0.6, 0.9, 1.0 and 1.1 suns-equivalent flux (as calibrated on a silicon reference cell) were used. The local series resistance image was calculated using an “A” image at 0.6 suns, and a sequence of “B” images at 1.0 suns (following the nomenclature of ref. [39]). To minimize the influence of hysteresis, and its impact on measurement time, the illumination level was adjusted at each bias point, from high to low, thus building all four IV curves in a single bias sweep. We found that the hysteresis response of the cell was most strongly affected by changing bias, with the cell more rapidly stabilizing at the second and subsequent illumination levels at fixed bias. Because of the slow stabilization of the cells, total measurement time was roughly 2.5 h for the MAPbI<sub>3</sub> PSC, and roughly 45 min for the multication PSC. However, this measurement time was the result of requiring data from many steady-state operating points for MLM verification and the slow transient photocurrent response of the cell. For typical series resistance calculations, only six images are required.<sup>[39]</sup> We can expect the total measurement time to decrease substantially for measurements intended for series resistance mapping only and with a faster transient photocurrent response (less hysteresis), which is becoming more common with higher performance perovskite compositions and solar cell structures.

At each operating point, PL images were captured at steady state. The luminescence signal is interpreted as a gauge of the local voltage

in the PSC. However, this relationship is complicated by two factors: (1) the possible presence of voltage-independent carriers, which contribute to luminescence emission, but not to the cell potential<sup>[42,51,52]</sup> and (2) luminescence emission from the FTO and TiO<sub>2</sub> surface layers, which is linearly dependent on illumination level. The latter is a problem distinct to the structure of many PSCs. Both factors are captured in short-circuit luminescence images, which can be subtracted from the positively biased PL images to reveal the luminescence signal from voltage-dependent carriers in the perovskite layer. At short circuit, there will still be a minimally positive potential across the junction because of the series resistance, but we expect that this potential is roughly 200–500 mV based on the final calculation of the cell's series resistance and short-circuit current, which predicts negligible emission from the perovskite layer. Therefore, all PL images used in these calculations were corrected using steady-state short-circuit images taken at equivalent illumination intensities. In addition, the standard corrections for the dark signal and the flat field were applied to all images. Spatial variation in illumination was measured at less than 5% based on measurements of the illumination flat field.

## Supporting Information

Supporting Information is available from the Wiley Online Library or from the author.

## Acknowledgements

This project received funding from the Australian Renewable Energy Agency ARENA. The views expressed herein are not necessarily the views of the Australian Government, and the Australian Government does not accept responsibility for any information or advice contained herein.

## Conflict of Interest

The authors declare no conflict of interest.

## Keywords

device characterization, luminescence, perovskite solar cells, series resistance

Received: June 4, 2017

Revised: July 22, 2017

Published online: September 18, 2017

- [1] H. J. Snaith, A. Abate, J. M. Ball, G. E. Eperon, T. Leijtens, N. K. Noel, S. D. Stranks, J. Wang, K. Wojciechowski, W. Zhang, *J. Phys. Chem. Lett.* **2014**, 5, 1511.
- [2] A. Dualeh, T. Moehl, N. Tétreault, J. Teuscher, P. Gao, M. K. Nazeeruddin, M. Grätzel, *ACS Nano* **2014**, 8, 362.
- [3] Y. Yuan, J. Chae, Y. Shao, Q. Wang, Z. Xiao, A. Centrone, J. Huang, *Adv. Energy Mater.* **2015**, 5, 1500615.
- [4] D. A. Jacobs, Y. Wu, H. Shen, C. Barugkin, F. J. Beck, T. P. White, K. Weber, K. R. Catchpole, *Phys. Chem. Chem. Phys.* **2017**, 19, 3094.
- [5] S. van Reenen, M. Kemerink, H. Snaith, *J. Phys. Chem. Lett.* **2015**, 6, 3808.
- [6] W. Tress, N. Marinova, T. Moehl, S. M. Zakeeruddin, M. K. Nazeeruddin, M. Grätzel, *Energy Environ. Sci.* **2015**, 8, 995.
- [7] T. M. Brenner, D. A. Egger, L. Kronik, G. Hodes, D. Cahen, *Nat. Rev. Mater.* **2016**, 1, 15007.
- [8] F. Brivio, K. T. Butler, A. Walsh, M. van Schilfgaarde, *Phys. Rev. B* **2014**, 89, 155204.
- [9] E. M. Hutter, M. C. Gélvez-Rueda, A. Osherov, V. Bulović, F. C. Grozema, S. D. Stranks, T. J. Savenije, *Nat. Mater.* **2016**, 16, 115.
- [10] T. Wang, B. Daiber, J. M. Frost, S. A. Mann, E. C. Garnett, A. Walsh, B. Ehrler, *Energy Environ. Sci.* **2017**, 10, 509.
- [11] M. Saba, M. Cadelano, D. Marongiu, F. Chen, V. Sarritzu, N. Sestu, C. Figus, M. Aresti, R. Piras, A. Lehmann, C. Cannas, A. Musinu, F. Quochi, A. Mura, G. Bongiovanni, *Nat. Commun.* **2014**, 5, 5049.
- [12] W. Tress, N. Marinova, O. Inganäs, M. K. Nazeeruddin, S. M. Zakeeruddin, M. Grätzel, *Adv. Energy Mater.* **2015**, 5, 995.
- [13] Z. Hameiri, A. Mahboubi Soufiani, M. K. Juhl, L. Jiang, F. Huang, Y.-B. Cheng, H. Kampwerth, J. W. Weber, M. A. Green, T. Trupke, *Prog. Photovoltaics Res. Appl.* **2015**, 23, 1697.
- [14] G. Lasher, F. Stern, *Phys. Rev.* **1964**, 133, A553.
- [15] P. Würfel, *J. Phys. C: Solid State Phys.* **1982**, 15, 3967.
- [16] P. Würfel, S. Finkbeiner, E. Daub, *Appl. Phys. A: Mater. Sci. Process.* **1995**, 60, 67.
- [17] U. Rau, *Phys. Rev. B* **2007**, 76, 85303.
- [18] G. El-Hajje, C. Momblona, L. Gil-Escrig, J. Ávila, T. Guillemot, J.-F. Guillemoles, M. Sessolo, H. J. Bolink, L. Lombez, *Energy Environ. Sci.* **2016**, 9, 2286.
- [19] S. D. Stranks, G. E. Eperon, G. Grancini, C. Menelaou, M. J. P. Alcocer, T. Leijtens, L. M. Herz, A. Petrozza, H. J. Snaith, *Science* **2013**, 342, 341.
- [20] S. D. Stranks, V. M. Burlakov, T. Leijtens, J. M. Ball, A. Goriely, H. J. Snaith, *Phys. Rev. Appl.* **2014**, 2, 34007.
- [21] A. M. Soufiani, M. J. Y. Tayebjee, S. Meyer, A. Ho-Baillie, J. S. Yun, R. W. MacQueen, L. Spiccia, M. A. Green, Z. Hameiri, *J. Appl. Phys.* **2016**, 120, 35702.
- [22] S. Mastroianni, F. D. Heinz, J.-H. Im, W. Veurman, M. Padilla, M. C. Schubert, U. Würfel, M. Grätzel, N.-G. Park, A. Hinsch, *Nanoscale* **2015**, 7, 19653.
- [23] A. M. Soufiani, Z. Hameiri, S. Meyer, S. Lim, M. J. Y. Tayebjee, J. S. Yun, A. Ho-Baillie, G. J. Conibeer, L. Spiccia, M. A. Green, *Adv. Energy Mater.* **2017**, 7, 1602111.
- [24] L. E. Mundt, F. D. Heinz, S. Albrecht, M. Mundus, M. Saliba, J. P. Correa-Baena, E. H. Anaraki, L. Korte, M. Grätzel, A. Hagfeldt, B. Rech, M. C. Schubert, S. W. Glunz, *IEEE J. Photovoltaics* **2017**, 7, 1081.
- [25] T. Trupke, R. A. Bardos, F. Hudert, P. Würfel, J. Zhao, A. Wang, M. A. Green, in *Proc. of the 19th European Photovoltaic Solar Energy Conf.*, Paris, France **2004**, pp. 758–61.
- [26] B. Hallam, B. Tjahjono, T. Trupke, S. Wenham, *J. Appl. Phys.* **2014**, 115, 44901.
- [27] S. Y. Lim, M. Forster, X. Zhang, J. Holtkamp, M. C. Schubert, A. Cuevas, D. Macdonald, *IEEE J. Photovoltaics* **2013**, 3, 649.
- [28] P. Würfel, T. Trupke, T. Puzzer, E. Schäffer, W. Warta, S. W. Glunz, *J. Appl. Phys.* **2007**, 101, 123110.
- [29] T. Fuyuki, H. Kondo, T. Yamazaki, Y. Takahashi, Y. Uraoka, *Appl. Phys. Lett.* **2005**, 86, 262108.
- [30] M. Saliba, T. Matsui, K. Domanski, J.-Y. Seo, A. Ummadisingu, S. M. Zakeeruddin, J.-P. Correa-Baena, W. R. Tress, A. Abate, A. Hagfeldt, M. Grätzel, *Science* **2016**, 354, 206.
- [31] J. Peng, T. Duong, X. Zhou, H. Shen, Y. Wu, H. K. Mulmudi, Y. Wan, D. Zhong, J. Li, T. Tsuzuki, K. J. Weber, K. R. Catchpole, T. P. White, *Adv. Energy Mater.* **2017**, 7, 1601768.
- [32] Y. Han, S. Meyer, Y. Dkhissi, K. Weber, J. M. Pringle, U. Bach, L. Spiccia, Y.-B. Cheng, *J. Mater. Chem. A* **2015**, 3, 8139.
- [33] G. E. Eperon, D. Moerman, D. S. Ginger, *ACS Nano* **2016**, 10, 10258.
- [34] G. Divitini, S. Caciovich, F. Matteocci, L. Cinà, A. D. Carlo, C. Ducati, *Nat. Energy* **2016**, 1, 15012.



- [35] H. Zhou, Q. Chen, G. Li, S. Luo, T.-B. Song, H.-S. Duan, Z. Hong, J. You, Y. Liu, Y. Yang, *Science* **2014**, 345, 542.
- [36] W. Chen, Y. Wu, Y. Yue, J. Liu, W. Zhang, X. Yang, H. Chen, E. Bi, I. Ashraf, M. Gratzel, L. Han, *Science* **2015**, 350, 944.
- [37] N. J. Jeon, J. Lee, J. H. Noh, M. K. Nazeeruddin, M. Grätzel, S. I. Seok, *J. Am. Chem. Soc.* **2013**, 135, 19087.
- [38] Z. Yu, L. Sun, *Adv. Energy Mater.* **2015**, 5, 1500213.
- [39] H. Kampwerth, T. Trupke, J. W. Weber, Y. Augarten, *Appl. Phys. Lett.* **2008**, 93, 202102.
- [40] A. G. Aberle, S. R. Wenham, M. A. Green, in *Conf. Record of the Twenty Third IEEE Photovoltaic Specialists Conf. (Cat. No. 93CH3283-9)*, IEEE, Louisville, KY **1993**; pp. 133–139.
- [41] K. C. Fong, K. R. McIntosh, A. W. Blakers, *Prog. Photovoltaics Res. Appl.* **2013**, 21, 490.
- [42] T. Trupke, E. Pink, R. A. Bardos, M. D. Abbott, *Appl. Phys. Lett.* **2007**, 90, 93506.
- [43] M. Glatthaar, J. Haunschild, M. Kasemann, J. Giesecke, W. Warta, S. Rein, *Phys. Status Solidi RRL* **2010**, 4, 13.
- [44] E. Franklin, K. Fong, K. McIntosh, A. Fell, A. Blakers, T. Kho, D. Walter, D. Wang, N. Zin, M. Stocks, E. Wang, N. Grant, Y. Wan, Y. Yang, X. Zhang, Z. Pheng, P. Verlinden, *Prog. Photovoltaics Res. Appl.* **2014**, 24, 411.
- [45] K. Schick, E. Daub, S. Finkbeiner, P. Würfel, *Appl. Phys. Solids Surf.* **1992**, 54, 109.
- [46] Y. Wu, H. Shen, D. Walter, D. Jacobs, T. Duong, J. Peng, L. Jiang, Y.-B. Cheng, K. Weber, *Adv. Funct. Mater.* **2016**, 26, 6807.
- [47] M. Wolf, H. Rauschenbach, *Adv. Energy Convers.* **1963**, 3, 455.
- [48] R. B. Dunbar, W. Moustafa, A. R. Pascoe, T. W. Jones, K. F. Anderson, Y.-B. Cheng, C. J. Fell, G. J. Wilson, *Prog. Photovoltaics Res. Appl.* **2016**, 25, 533.
- [49] J. Peng, Y. Wu, Y. Wang, D. Jacobs, H. Shen, X. Fu, Y. Wan, T. Duong, N. Wu, C. Barugkin, H. T. Nguyen, D. Zhong, J. Li, T. Lu, Y. Liu, M. Lockrey, K. Weber, K. Catchpole, T. P. White, *Energy Environ. Sci.* **2017**, <https://doi.org/10.1039/C7EE01096F>.
- [50] D. Walter, A. Fell, E. Franklin, D. Macdonald, B. Mitchell, T. Trupke, *IEEE J. Photovoltaics* **2014**, 4, 368.
- [51] M. K. Juhl, T. Trupke, *J. Appl. Phys.* **2016**, 120, 165702.
- [52] M. Kasemann, D. Grote, B. Walter, W. Kwapil, T. Trupke, Y. Augarten, R. a. Bardos, E. Pink, M. d. Abbott, W. Warta, *Prog. Photovoltaics Res. Appl.* **2008**, 16, 297.
- [53] B. Michl, M. Kasemann, J. Giesecke, M. Glatthaar, A. Schütt, J. Carstensen, H. Föll, S. Rein, W. Warta, H. Nagel, *Proceedings of the 23<sup>rd</sup> European Photovoltaic Solar Energy Conference*, Valencia, Spain, **2008**, p. 1176–1181.